Journal of Membrane Science 628 (2021) 119276

Contents lists available at ScienceDirect

Journal of Membrane Science

journal homepage: http://www.elsevier.com/locate/memsci

Fast water transport through biomimetic reverse osmosis membranes embedded with peptide-attached (pR)-pillar[5]arenes water channels

Yu Jie Lim [a,b,c], Kunli Goh [a], Gwo Sung Lai [a], Chiann Yi Ng [a,b], Jaume Torres [a,d], Rong Wang [a,b,*]

[a] Singapore Membrane Technology Center, Nanyang Environment and Water Research Institute, Nanyang Technological University, 637141, Singapore
[b] School of Civil and Environmental Engineering, Nanyang Technological University, 639798, Singapore
[c] Interdisciplinary Graduate Programme, Graduate College, Nanyang Technological University, 637553, Singapore
[d] School of Biological Sciences, Nanyang Technological University, 637551, Singapore

ARTICLE INFO

Keywords:
Biomimetic membrane
Synthetic water channels
Peptide-attached (pR)-pillar[5]arenes
Interfacial polymerization

ABSTRACT

This study examined the feasibility and performance of a nanochannel-based biomimetic membrane (NBM) for brackish reverse osmosis (RO) desalination. Two types of peptide-attached synthetic nanochannels, (pR)-pillar[5]arenes (pRPH) and (pS)-pillar[5]arenes (pSPH), were incorporated into liposomes. pSPH is a diastereomer of pRPH and was used as a negative control (*i.e.* mutant) to pRPH in this work. The nanochannel-containing liposomes (*e.g.* pRPH-liposomes) were then immobilized into the active layer of the RO membranes via *in situ* interfacial polymerization on the top of a polysulfone support membrane to form NBM-pRPH membranes. To maximize the potential and benefits of the NBM-pRPH membrane, the physical characteristics of the polyamide layer was further tuned using some additives and the eventual membrane was named as NBM-pRPH-A. The NBM-pRPH-A membrane exhibited a water permeability of 6.09 L m^{-2} h^{-1} bar^{-1} and 98.2% NaCl rejection under a 15.5 bar applied pressure using 2000 mg L^{-1} as feed solution. The 62% flux increment with respect to the pristine control is postulated to arise from a thinner, less cross-linked (more free volume) and more hydrophilic active layer as well as the possible supplementary transport pathways of the pRPH-liposomes. The performance of the NBMs under differential feed pressures and temperatures further exemplifies the water permeation property of the pRPH nanochannels. Accordingly, the NBM-pRPH-A gave a water permeability higher than commercial RO membranes tested in this work (DuPont BW30 and Hydranautics ESPA2) as well as other RO membranes reported in the literature. This study provides a tangible foundation for the development of NBMs for brackish RO desalination.

1. Introduction

Freshwater is crucial for the survival of mankind. However, this precious resource is becoming perilously scarce due to anthropogenic stressors such as population growth, rapid industrialization and climate change [1]. To address the grand challenge of water scarcity, it is essential to tap on water sources beyond what is available from the hydrological cycle. In the past 50 years, desalination has evolved as a promising strategy that allow us to tap on unconventional resources like brackish water and seawater. Today, the most widely adopted desalination technology is reverse osmosis (RO), which utilizes semi-permeable membranes capable of separating water and dissolved solutes. The state-of-the-art commercial RO membranes consists of an ultrathin dense polyamide layer (~200 nm) laminated on a microporous sublayer, whereby the former is the separation (or selective) layer and the latter provides the mechanical strength needed to endure high pressures [2].

Because of the solution-diffusion transport mechanism, where the permselectivity of an RO membrane is determined by the differences between the dissolution and diffusion rates of water/salt through the polyamide layer, empirical evidence has suggested that RO membranes exhibit a recurring permeability-selectivity tradeoff that renders them difficult to achieve higher water permeability using conventional polymeric materials [3,4]. Nanotechnology-enabled membranes have brought about the development of ultrapermeable membranes (UPMs) capable of producing much higher water flux than the conventional

* Corresponding author. Singapore Membrane Technology Center, Nanyang Environment and Water Research Institute, Nanyang Technological University, 637141, Singapore.
E-mail address: rwang@ntu.edu.sg (R. Wang).

https://doi.org/10.1016/j.memsci.2021.119276
Received 6 February 2021; Received in revised form 7 March 2021; Accepted 8 March 2021
Available online 17 March 2021

TFC-RO membranes [5]. UPMs are based on the idea of incorporating nanomaterials with high intrinsic permselectivity into the ultrathin polyamide layer to give thin-film nanocomposite (TFN) membranes, which have been suggested as the "next-generation" membrane capable of transcending the permeability-selectivity tradeoff (*e.g.* by outperforming the classical RO membranes) [6,7]. Typical nanomaterials used in the fabrication of TFN membranes include filler materials such as carbon-based materials [8], zeolites, silica and metal-organic frameworks (MOFs) [7]. However, there are inherent issues involved in the fabrication of TFN membranes. For example, the poor compatibility between inorganic filler materials and the polyamide material can result in the formation of non-selective voids (defects) in the polyamide layer, thereby leading to a drastic drop in the selectivity of TFN membranes, which is an unacceptable outcome. A defect is defined as an area on the membrane in which the PA selective layer is absent or has cracks, such that the underlying support layer is directly exposed to the feed water [9].

Recent developments in material synthesis and self-directed assembly have opened up the possibility of engineering the selective layer of RO membranes at the molecular scale. The biomimetic RO membrane is one such example, which typically involves biological elements or adopted concepts from biological systems to incorporate water channels in "bioinspired" membranes [10]. Biomimetic RO membranes are gaining traction over the years, owing to their compatibility with the polyamide layer and the enhanced water permeability that comes with uncompromised membrane selectivity [11]. One of the most prominent nanomaterials used in the fabrication of biomimetic membranes is aquaporin (AQP), a sub-nanometer water channel that has been widely studied due to its intrinsically high permeability and selectivity [7,10]. To mimic its biological environment, AQPs are typically incorporated into lipid bilayers, and one approach is to immobilize the AQP-vesicles into the selective layer to form AQP-based biomimetic membranes. However, there remains unresolved challenges at the current stage, such as protein instability in the long-term and poor processability of AQPs as well as limited enhancement in membrane performance [9,12].

Herein, we propose a synthetic nanochannel-based biomimetic membrane (NBM) as an alternative to AQP-based biomimetic membrane to address these challenges [12,13]. According to theoretical concepts, it is possible to design synthetic water nanochannels that mimic the characteristics and superb transport properties of AQPs, but these channels must be easily processable, relatively stable and have high intrinsic water-salt permselectivity [6]. Peptide-appended pillar[5]arene (pRPH) nanochannel is a single-molecule synthetic channel that fits the bill by showing ready insertion and self-alignment within lipid bilayers [6]. Pillar[5]arenes are cyclic macromolecules consisting of five hydroquinone groups connected in the para-positions by methylene bridges [14]. In peptide-appended pillar[5]arene channels (*e.g.* pRPH), the macrocycle, which fairly resembles a carbon nanotube (CNT), determines the pore diameter (~0.5 nm) [15], whereas the peptide-appended arms govern the length of the channel. Hydrogen bonding between the peptide arms is known to provide stability to the peptide-appended arms which makes pillar[5]arenes a superb template that can be functionalized into tubular nanostructures [15]. Analogous to AQPs, the pore diameter of pRPH (~0.45 nm at the constriction zone) supports the single file transport of water molecules [16]. In general, the fast water transport through pillar[5]arenes channel is surmised to arise from its hydrophobic interior [12]. Because of its ability to mimic CNTs and AQPs, many research works have sought to incorporate pillar[5]arenes into membranes with the aim of enhancing the latter's water permeability. Some prominent attempts include the use of pillar[5]arene channels in lipid bilayer membranes [15,17], block copolymer membranes (*via* layer-by-layer deposition of 2D sheets) [18] and supported lipid membrane (*via* liposome fusion) [16]. However, there has been no report of the incorporation of pillar[5]arenes channels into the dense selective layer of RO desalination membranes.

Hence, in this work, we incorporated pRPH nanochannels into liposomes (*i.e.,* lipid vesicles) to form pRPH-liposomes, which were then immobilized into the polyamide selective layer (Fig. 1). The pRPH water channels in the liposomes are envisaged to improve the membrane permeability, while the good compatibility between the liposomes and polyamide gives rise to the formation of a defect-free polyamide active layer, offering uncompromised membrane selectivity and resolving the aforementioned challenges. To the best of our knowledge, this work is the first to demonstrate the feasibility and performance of RO membranes embedded with pillar[5]arene channels *via* the vesicle-based approach. The successful fabrication of synthetic nanochannel-based RO membranes is expected to open up new avenues for high-performance TFN membranes for desalination.

2. Experimental

2.1. Materials and chemicals

Milli-Q deionized (DI) water (18.3 MΩ cm) was used in the preparation of aqueous solutions. Unless otherwise mentioned, all chemicals were purchased from Sigma-Aldrich. Polysulfone beads (PSf, Solvay Specialty Polymers) together with solvents 1-Methyl-2-pyrrolidinone (NMP) and Dimethylformamide (DMF) were used in the preparation of support membranes. 1,2-Dioleoyl-sn-glycerol-3-phosphocholine (DOPC) lipids (in chloroform, Avanti Polar Lipids) and phosphate buffered saline (PBS) solution (Thermo Fisher Scientific, MA, USA) were used to prepare DOPC liposomes. Two types of synthetic nanochannels, peptide-attached (pR)- and (pS)-pillar[5]arenes, denoted as pRPH and pSPH, respectively, were used in the preparation of liposomes with nanochannels. pSPH is a diastereomer of pRPH and is used as a mutant (negative control) to pRPH in this work. The detailed synthesis procedure and properties of pRPH and pSPH nanochannels are outlined in our previous work [16]. Sucrose was used as the draw solution in the stopped-flow experiments. Trimesoyl chloride (TMC) and m-Phenylenediamine (MPD) were used to synthesize the polyamide active layer *via* interfacial polymerization (IP). N-hexane was used as the organic solvent to dissolve TMC. Triethylamine (TEA), Camphorsulfonic acid (CSA) and Dimethyl sulfoxide (DMSO) were used as aqueous phase additives in IP. Two state-of-the-art commercial RO membranes (DuPont Filmtec BW30 (USA) and Hydranautics ESPA2 (USA)) were tested in this study for benchmarking purposes.

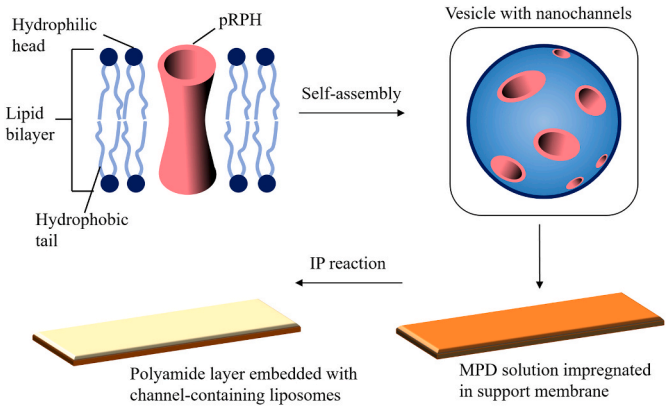

Fig. 1. Schematic illustration of the synthesis of NBMs via interfacial polymerization. The pRPH nanochannel (red) is inserted and self-aligned into lipid bilayers. The liposomes were mixed with the MPD aqueous solution before the porous support membrane was immersed in the MPD solution. The support membrane impregnated with MPD solution reacted with TMC in IP to form the polyamide layer. (For interpretation of the references to colour in this figure legend, the reader is referred to the Web version of this article.)

2.2. Liposome preparation

The liposome containing pure DOPC (*i.e.* no nanochannels) is the control liposome. The pRPH and pSPH nanochannels were incorporated into the DOPC lipid vesicles *via* the film rehydration technique [19,20], and are termed as pRPH-liposomes and pSPH-liposomes in this work. Briefly, 400 mg of DOPC lipid dissolved in 16 mL of chloroform was dried under a nitrogen head space to form a thin lipid film on the inner surface of a glass vial. The glass vial was then stored in a vacuum desiccator for 12 h to ensure complete removal of chloroform. Subsequently, 40 mL of PBS buffer solution and a certain amount of nanochannels (lipid to channel ratios (LCRs) of 100, 200, 300 and 400) were added into the glass vial and agitated for 1 h, prior to three cycles of freeze-thaw to form unilamellar liposomes. The resultant liposome solution was then extruded (GJE Jacketed Liposome Extruder, Genizer, USA) three times each using polycarbonate filters (Whatman, USA) with pore sizes of 200 nm and 100 nm to obtain liposomes with uniform size distribution.

2.3. Biomimetic membrane synthesis

The microporous support membranes were fabricated by a phase inversion method according to our previous works [21–23]. Briefly, the dope solution (10 wt% PSf, 11.3 wt% NMP and 78.7 wt% of DMF) was stirred at 65 °C, degassed and cooled down to ambient temperature prior to casting. First, the nonwoven fabric was fixed onto the fully dry and clean glass plate using adhesive tapes. Next, a micrometer film applicator (Elcometer 3570, UK) with a gate height of 200 μm was used to evenly spread the dope solution on the nonwoven fabric. The glass plate was then immediately immersed into the coagulant bath (tap water at ambient temperature) to form the PSf support membranes.

The polyamide active layer was synthesized on the top of the support membrane using IP methodology. Briefly, three solutions were employed in the IP process: MPD aqueous solution, 0.1% TMC solution, and pure hexane. The concentration of MPD was fixed at 2% throughout, and the pristine TFC control membrane was made from the 2% MPD solution. To isolate the influence of liposomes in affecting the RO membrane permselectivity, a systematic optimization of the liposome concentration (at fixed LCR) and the LCR (at fixed liposome concentration) were performed to identify the best performance achievable by the biomimetic membranes. The membrane incorporated with pure DOPC liposomes was denoted as TFC-DOPC, whereas the NBMs incorporated with pRPH- and pSPH-containing liposomes were labeled as NBM-pRPH and NBM-pSPH, respectively. Based on the optimized liposome concentration and LCR, some additives were added into the MPD aqueous phase in an attempt to further enhance the permselectivity of the biomimetic membrane. The additives are DMSO and TEACSA salt [24]. The NBMs made with additives were labeled as NBM-pRPH-A and NBM-pSPH-A.

The exact IP procedure was adopted as reported previously [21–23]. In brief, the PSf supports were immersed in MPD solutions for 1 min and thereafter the excess MPD solution was removed using a rubber roller. Next, the MPD-impregnated PSf supports were immersed in TMC solution for 1 min before rinsing with pure hexane solution. Thereafter, the membranes were thermally cured at a 60 °C oven for 10 min to induce further polymerization and cross-linking of the active layer.

2.4. Liposome characterization

The size distributions of the vesicles in the liposomes were determined using a Nano Zetasizer (ZEN3600, Malvern Panalytical, UK). The water permeability of the nanochannel containing vesicles was characterized by an SX20 Stopped Flow Spectrometer (Applied Photophysics, UK). The stopped flow test was conducted under the fluorescence kinetic mode and the wavelength of the light source was 500 nm. The vesicle solution and draw solution (0.6 M sucrose) were mixed in a 1:1 ratio under 5 bar pressurized nitrogen gas with a dead time of 500 μs. The volume reduction of the vesicle as a result of outward water transport was monitored by a light scattering method. The fitted rate constant k (which is an indicator of the volumetric shrinkage rate) was calculated by the Pro-Data SX software using a single exponential fitting function. The water permeability of each vesicle was calculated as follows:

$$P_f = \frac{k}{S/V_0 \times V_w \times \Delta osm} \quad (1)$$

where S/V_0 is the ratio of surface area to initial volume of each vesicle, V_w is the partial molar volume of water (0.018 L/mol), and Δosm is the difference in osmolarity between the intravesicular and draw solutions.

2.5. Membrane characterization

All membrane samples were air-dried at ambient temperature for at least 24 h prior to characterization. The surface morphology and cross-sections of the membranes were characterized using FESEM (Field-emission scanning electron microscopy, JSM-7600F, JEOL, Japan) at 5.0 kV. For cross-sectional analysis in FESEM, the membranes were immersed in liquid nitrogen for at least 3 min before freeze fracturing. The nonwoven fabrics were manually peeled off from the back side of the membrane using a sharp tweezer. Prior to analysis in FESEM, the samples were sputter-coated (JEC-1600, JEOL, Japan) with a thin platinum layer for 90 s at 20 mA. The active layer height was measured using Image J analysis software at five arbitrary locations for each cross-sectional image in SEM. The cross-section images of the polyamide layers were captured by transmission electron microscopy (TEM, JEM-1400, JEOL, Japan) at an accelerating voltage of 120 kV. The samples were embedded in epoxy resin and the resin capsules were subjected to curing at 60 °C for 24 h. Thereafter, approximately 60 nm thick sections were sectioned by an ultramicrotome (Ultracut UCT, Leica, Germany) with a diamond knife and transferred to copper grids for TEM observation. Scanning Transmission Electron Microscopy (STEM) combined with Energy Dispersive X-ray spectroscopy (STEM-EDX) was used to obtain elemental mapping of the polyamide layers.

The roughness average (R_a) of all membranes were measured using AFM (Atomic force microscope, Park XE-100, Park Systems, Korea) in a non-contact mode using the PPP-NCHR cantilever (Non-contact cantilever with high resonant frequency, Nanosensors, Switzerland) with a frequency and elastic modulus of 330 kHz and 42 N/m, respectively. The scanning area was 5 × 5 μm with a resolution of 256 pixels. A contact angle goniometer (OCA15, DataPhysics Instruments, Germany) was used to measure the surface wettability of all membranes using the sessile drop method. In brief, a droplet of 3 μL of DI water was released onto the dry membrane surface, and an image of the droplet in equilibrium with the membrane surface was taken. The contact angle was computed based on six equilibrium measurements (averaged by the left and right angles) using SCA20 software.

The attenuated total reflection-fourier transform infrared (ATR-FTIR) spectrometer (IR, Prestige-21, Shimadzu, Japan) was used to analyze the functional groups in the active layer of all membranes. The baseline-corrected spectra (ranging from 400-4000 cm^{-1}) were collected on a FTIR with a sampler over 32 scans at a resolution of 4 cm^{-1}. XPS (X-ray photoelectron spectroscopy, Kratos Analytical, AXIS Supra, UK) was used to determine the surface elemental compositions of the membranes using a monochromatic aluminium ultraviolet source (1486.6 eV). The survey spectra from 0-1400 eV were collected and the obtained data were analyzed using CasaXPS software. The binding energy of all elements were calibrated with respect to the C1s peak at 284.8 eV. The cross-linking degrees of the membrane active layers were estimated using two methods: 1) the N/O ratio in XPS and 2) the intensity of the unreacted acyl chloride peak at 950 cm^{-1} in FTIR analysis (plot of transmittance against wavenumber) [21,23,25]. It is noted that the nanochannels contain elements N and O, and thus might affect the

N/O ratio in XPS. Nevertheless, the cross-linking degree can still be estimated *via* XPS [26,27] because there is only a trace amount (~0.002 wt% in MPD phase) of nanomaterials present in the PA layer (*i.e.,* elements N and O detected by XPS should be dominated by the bulk PA layer consisting of the MPD-TMC chemistry).

2.6. Membrane filtration test

All membrane coupons were soaked in DI water for at least 12 h prior to testing. The RO membranes were evaluated using a bench-scale cross-flow filtration setup equipped with permeation cells (CF042D, Sterlitech, Kent, WA, USA). The active membrane area of each coupon is 42 cm^2. The RO performance tests were conducted using 2000 mg·L^{-1} NaCl feed solution (pH = 7) at a hydraulic pressure of ~15.5 bar. The feed solution temperature was kept constant at 25.0 ±0.5 °C by a chiller (PolyScience, Niles, IL, USA). The membranes were pressurized at 20% higher pressure (~18.5 bar) for 1 h prior to data collection. The commercial BW30 and ESPA2 membranes were tested in parallel for comparison purposes.

The water flux (J_w) (L m^{-2} h^{-1}; LMH) was calculated based on the gravimetric method, by measuring the amount of permeate collected in a specified time interval. The salt rejection (R) was calculated based on the concentration difference between the permeate (C_p) and feed (C_f) measured using a conductivity meter (Ultrameter II, Myron L Company, USA):

$$R = 1 - C_p/C_f \tag{2}$$

The water and salt permeability coefficients (denoted as A and B respectively) were calculated according to the following equations:

$$A = \frac{J_w}{(\Delta P - \Delta\pi)} \tag{3}$$

$$B = J_w \times \left(\frac{1-R}{R}\right) \tag{4}$$

where ΔP and $\Delta\pi$ corresponds to the applied hydraulic pressure and the osmotic pressure difference across the semi-permeable membrane.

3. Results and discussion

3.1. Characteristics of the liposomes

DOPC lipid was selected to incorporate the nanochannels to form liposomes due to its excellent stability with solute ions. In addition, DOPC liposomes are known to be fairly stable (*i.e.,* should not deform) under high pressure and temperature. Dynamic light scattering measurements showed that the liposomes have an average size of 120 ± 6 nm with a polydispersity index of 0.093 ± 0.026. The small polydispersity index reflects the even size distribution of vesicles which ensures the accuracy of determining water permeability in stopped-flow tests [19]. Fig. 2A presents the curves with a sharp increment in fluorescence followed by a stable stage for the pRPH-liposomes (k ~ 90 – 245 s^{-1}). The rapid increase of the signal within a short period (<0.025 s) indicates an ultrafast transport of water molecules across the pRPH channels, while the ensuing stable stage of the signal suggests the good stability of the liposomes under the current solute environment [15,16]. Contrastingly, the DOPC liposomes (Fig. 2A) and pSPH-liposomes (Fig. 2B) only showed gradual increment with small k values (~ 10 – 15 s^{-1}), thereby confirming the impermeable nature of both liposomes [28]. Since identical procedures were used in the preparation of all

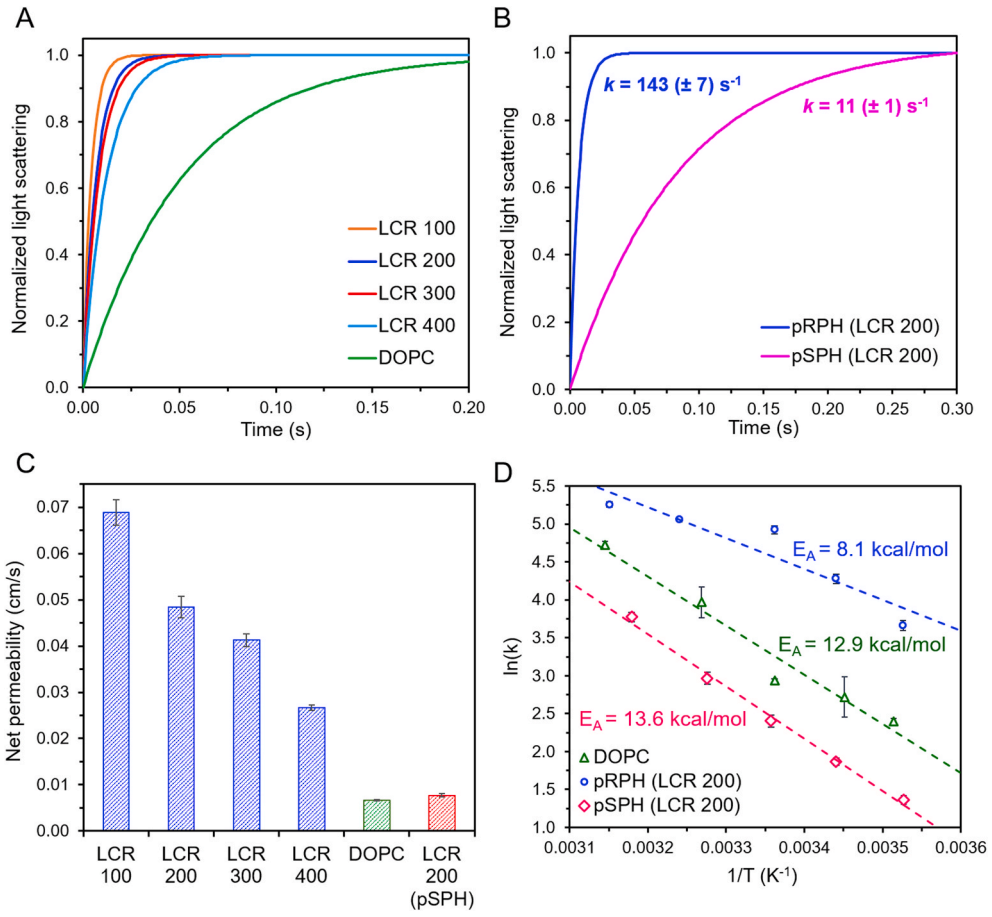

Fig. 2. (A) Stopped-flow light scattering curves of pRPH-liposomes (different LCRs) and DOPC liposome at 25 °C. **(B)** Stopped-flow light scattering curves of pRPH-liposome and pSPH-liposome (LCR 200). For (A) and (B), the liposomes were exposed to a hypertonic solution of 0.6 M sucrose. **(C)** The net water permeability of the pRPH-liposomes (different LCRs), DOPC liposome and pSPH-liposome (LCR 200) measured under hypertonic conditions at 25 °C. **(D)** Arrhenius plots for determining the activation energy (E_A). The rate constants of the liposomes were obtained by exposing them to a hypertonic solution of 0.6 M sucrose at different temperatures. The activation energies were calculated from the slope of the best-fit lines. Error bars: 3 or more independent samples.

liposomes and the pSPH-liposome (mutant) was used as a negative control, it is evident that water transport across the pRPH-liposome is channel mediated.

The net permeability of each vesicle in the liposomes are tabulated in Fig. 2C, which shows that the water permeability of the pRPH-liposome increased with pRPH load. When the LCR was 200, the net permeability of a pRPH-containing vesicle is 0.0485 cm s^{-1}, which is 6 times higher than that of the pSPH-containing vesicle (0.0077 cm s^{-1}), thereby reaffirming the water permeation property of the pRPH nanochannels. In addition, the activation energies (E_A) obtained from the best fit lines in the Arrhenius plots (Fig. 2D) revealed that the addition of the pRPH nanochannels into the liposomes reduced the activation energy (12.9 – 13.6 kcal/mol for the control) to 8.1 kcal/mol. This is another good evidence that water transport across the pRPH-liposomes was facilitated by the pRPH nanochannels [16].

3.2. Characteristics of the biomimetic membranes

3.2.1. Membranes embedded with liposomes

In an attempt to optimize the liposome concentration in MPD phase, different amounts of pRPH-liposomes were added into the MPD solution. Fig. 3A and B shows that the polyamide height and roughness remained fairly consistent when the pRPH-liposome concentration was varied from 0 mg/mL (control membrane) to 0.75 mg/mL. Further increase in pRPH-liposome concentration (1.0 mg/mL) led to an observable increase in the height and roughness of the active layer. It is hypothesized that the vesicles could have aggregated at high concentration of 1.0 mg/mL thereby leading to the formation of bigger globules. The presence of bigger globules and protuberances led to a much rougher active layer [19]. Similarly, the active layer became spatially thicker (in terms of height) because of the agglomeration of the vesicles.

Fig. 3C and D presents the cross-linking degrees of the biomimetic membranes made with different pRPH-liposome concentrations in the form of N/O ratio analysis in XPS and the intensity of the FTIR spectra at 950 cm^{-1}, respectively. According to the literature, the N/O ratio of a polyamide with a fully cross-linked structure and fully linear structure is 1 and 0.5, respectively [21]. It is noticed that the cross-linking degree remained fairly constant for liposome concentrations of 0 – 0.75 mg/mL, but decreased slightly at high pRPH-liposome concentration of 1.0 mg/mL (*i.e.* the active layer became looser) (Fig. 3C and D). This observation can be explained by the presence of bigger globules at high vesicle concentrations, which led to the formation of more voids in the polyamide active layer [19,20]. Consequently, the free volume in the active layer increases, thereby leading to a lower cross-linking degree.

Next, we attempt to study the active layer characteristics of TFC-DOPC and biomimetic membranes NBM-pRPH and NBM-pSPH at a fixed liposome concentration in MPD solution. Fig. 4 shows that the surface morphologies are fairly similar for all three membranes, with the classical ridge and valley structure which is a characteristic of polyamide made from the MPD-TMC chemistry. The active layer heights for all three membranes are ~215 nm. The roughness and contact angle of the active layer are similar at ~45 nm and ~60°, respectively. Thus, it can be concluded that the polyamide matrices of these three membranes are similar in terms of physical characteristics.

To provide empirical evidence of liposomes incorporation in the polyamide layer, the cross-section of the NBM-pRPH membrane was

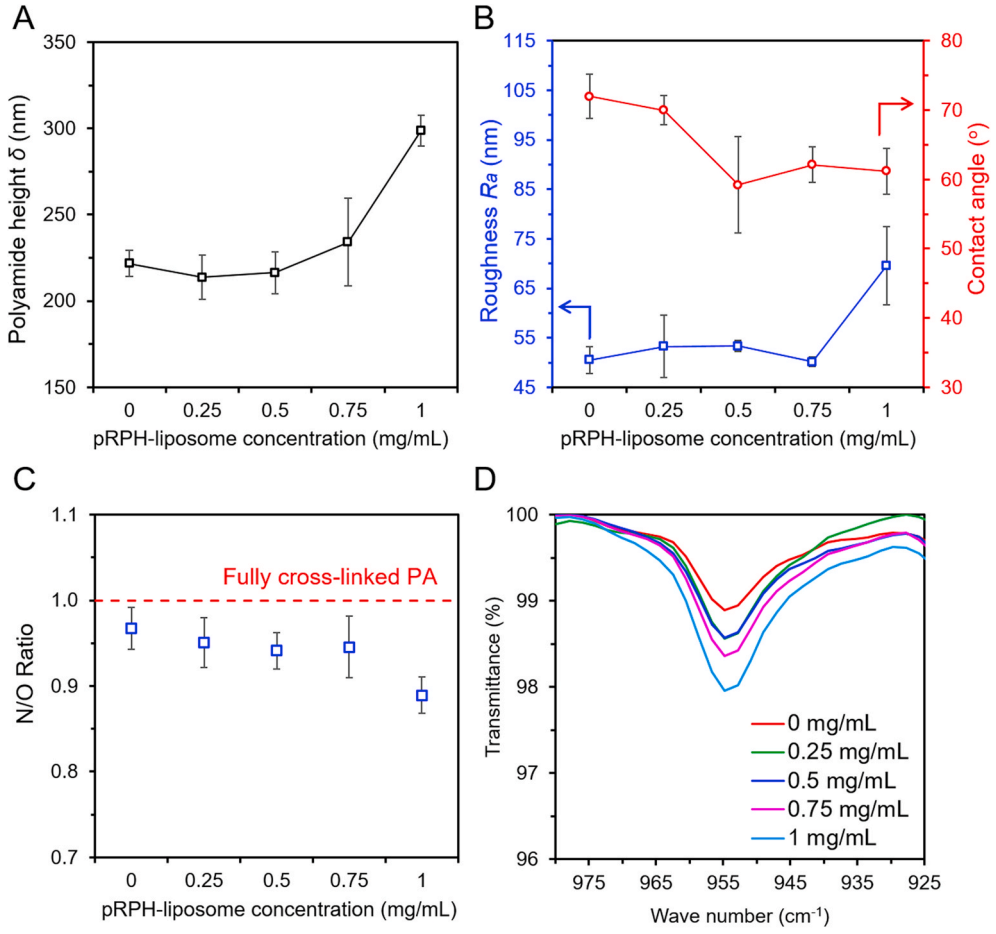

Fig. 3. The polyamide layer properties for biomimetic membranes prepared with various pRPH-liposome concentrations at fixed LCR 200. **(A)** Polyamide height. **(B)** Polyamide roughness and contact angle. **(C)** Cross-linking degree in XPS presented in terms of the N/O ratio. **(D)** FTIR spectra at 950 cm^{-1}. Error bars: 3 or more independent samples.

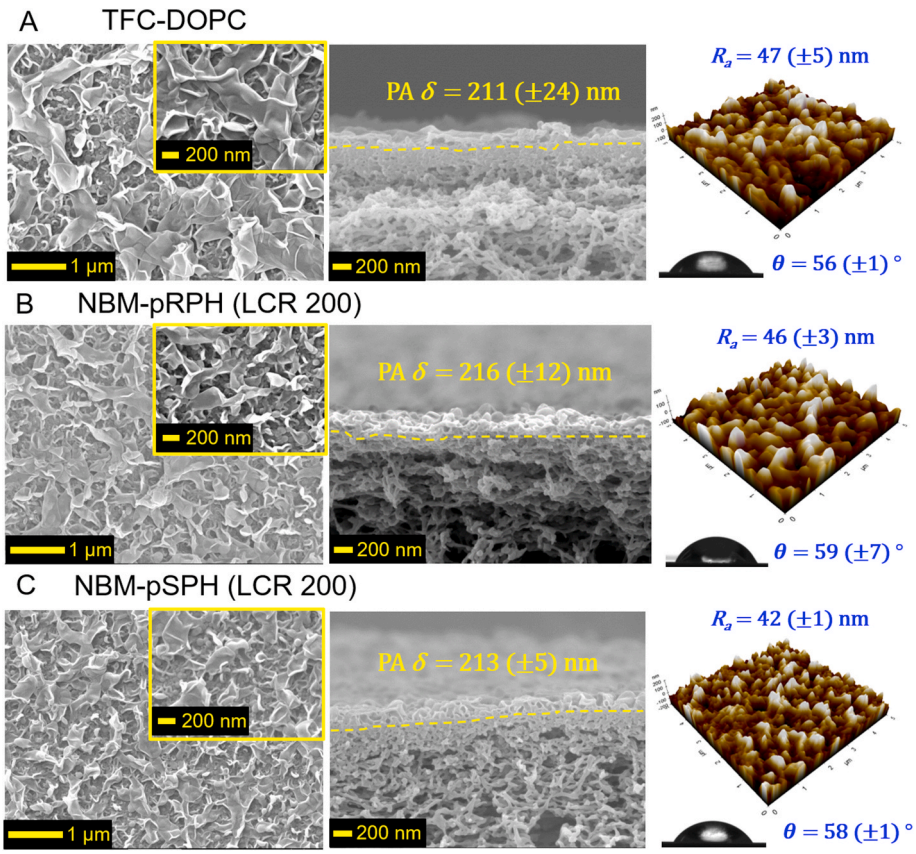

Fig. 4. The polyamide layer properties of the biomimetic membranes incorporated with **(A)** DOPC liposome, **(B)** pRPH-liposome (LCR 200) and **(C)** pSPH-liposome (LCR 200). The liposome concentration in MPD phase is 0.5 mg/mL. **Left images:** surface morphologies in SEM. **Middle images:** SEM cross-sectional images with the active layer height (δ). **Right images:** 3D AFM images with roughness average (R_a) and contact angle (θ) analysis. Error bars: 3 or more independent samples.

imaged using TEM. The TEM images in Fig. 5A and B revealed dark and sharp-edged features which were proven to be DOPC liposomes using spatially resolved analytical tools such as STEM-EDX [26]. Elemental mapping of sulfur and nitrogen (Fig. 5C and D respectively) on the NBM-pRPH membrane shows the polyamide layer (~200 nm in height) on top of the PSf support, which is consistent with the measurements in SEM (Fig. 4). The dark-shaped features in Fig. 5B gave intense phosphorous signal (evidenced in Fig. 5E), suggesting the presence of DOPC (*i.e.* not present in MPD and TMC monomers), which gives good evidence of successful DOPC incorporation into the polyamide layer. However, it is noticed that the features are not circular in shape and their sizes did not match that of lipid vesicles measured using zetasizer (see Section 3.1). We attributed these irregularities to the deformation of DOPC liposomes during polyamide layer formation and the inevitable contraction that followed when drying the membrane and subjecting it to high vacuum during TEM characterization. Also, the pRPH nanochannels could not be directly observed in SEM or TEM images, probably because of the small sizes (1–3 nm) and low concentration in the

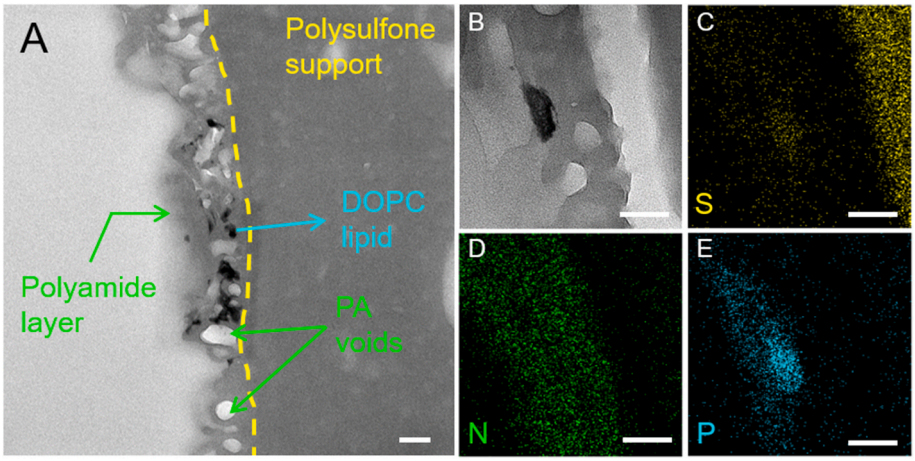

Fig. 5. Cross-sectional TEM images of the polyamide layer of **(A, B)** NBM-pRPH at low and high magnifications. The yellow dotted lines corresponds to the boundary between the polyamide and support layers. (B) was selected for STEM-EDX elemental mapping in **(C, D, E),** corresponding to the mappings of sulfur, nitrogen and phosphorous. Scale bars: 100 nm. (For interpretation of the references to colour in this figure legend, the reader is referred to the Web version of this article.)

polyamide layer [29].

After we ascertained the successful incorporation of the lipid vesicles, the chemical characteristics of TFC-DOPC, NBM-pRPH and NBM-pSPH were examined *via* FTIR and XPS analyses. First, the ATR-FTIR spectra (Fig. 6A) showed three peaks that are characteristics of the polyamide matrix made from the MPD-TMC chemistry. Specifically, the peaks at ~1610 cm^{-1} are thought to be attributed to the stretching vibrational motion of the C=C bonds [30,31], whereas the peaks at ~1665 cm^{-1} and 1538 cm^{-1} can be attributed to the amide I bonds and amide II bonds [32], respectively. In a bid to deduce the changes in the chemistry of the polyamide layers, XPS analyses were carried out for all three membranes *via* the deconvolution of the C1s high resolution peaks to give a representation of different functional groups present (Fig. 6B–D). It is noticed that all three membranes (TFC-DOPC, NBM-pRPH, NBM-pSPH) exhibited three major peaks at 284.8 eV, 286.2 eV and 288.2 eV. According to the literature, the peak at 284.8 eV is assigned to the carbon atom in C–C and C–H bonds [30]. The intermediate peak at 286.2 eV is thought to be assigned to carbon atoms associated with weak electron withdrawing groups (*e.g.* carbon in C–N bond) [30]. Thirdly, the peak at ~288.2–288.5 eV is assigned to carbon atoms associated with strong electron-withdrawing atoms (*i.e.,* carbons in amides bond O=C–N and pendant carboxylic acid groups O=C–O) [33]. However, the NBM-pRPH and NBM-pSPH exhibited one more peak at ~285.5 eV as compared to TFC-DOPC (Fig. 6C and D). The peak at 285.5 eV is known to be associated with the ether bonds (C–O–C) [34]. The distinctive existence of the peak at 285.5 eV for NBM-pRPH and NBM-pSPH are reminiscence of the unique ether bonds present in pRPH and pSPH nanochannels [16], providing good evidence that both pRPH and pSPH nanochannels were successfully embedded into the PA active layer.

3.2.2. Membranes embedded with liposomes and additives in aqueous phase

Fig. 7A and B presents the physical characteristics of the NBM-pRPH-A and NBM-pSPH-A membranes, respectively. As shown in Fig. 4, the polyamide matrices are fairly identical for both membranes in terms of the surface morphology, height, roughness and hydrophilicity. However, with the incorporation of additives in the MPD solution, it is noticed that the height of the polyamide layer reduced drastically (from ~215 nm to ~150 nm), whereas the roughness decreased by ~15% (from ~46 nm to ~39 nm). We attributed this to the effect of additives DMSO and TEACSA during the IP process. Being a polar aprotic organic solvent, DMSO is known to form dipole-dipole interaction with TMC during IP, thereby increasing the TMC concentration at the reaction interface [23]. Consequently, the IP reaction rate was higher and the diffusion barrier was formed earlier (*i.e.* MPD diffusion towards the organic phase was impeded at a shorter timescale). The growth of the polyamide layer was therefore terminated prematurely, giving rise to a thinner and smoother active layer [23]. Also, the incorporation of hydrophilic salt TEACSA in the aqueous phase was known to catalyze the IP reaction, resulting in the formation of a thinner active layer since the polyamide growth was completed in a shorter timescale [35,36].

Secondly, it was observed that the NBM-pRPH-A and NBM-pSPH-A possessed a more hydrophilic surface as evidenced by the lower contact angles (~48°) in Fig. 7A and B, as compared to the membranes made without additives (Fig. 4). It was hypothesized that the addition of TEACSA in the MPD solution increased the hydrophilicity of the NBMs because of its inherently abundant sulfonyl hydroxide groups [24,36]. Thirdly, the cross-linking degrees of the NBM-pRPH-A and NBM-pSPH-A were much lower than their counterparts made without the additive as evidenced by the much lower N/O ratio (Fig. 7C). This observation is expected, considering that the dipole-dipole interaction between DMSO

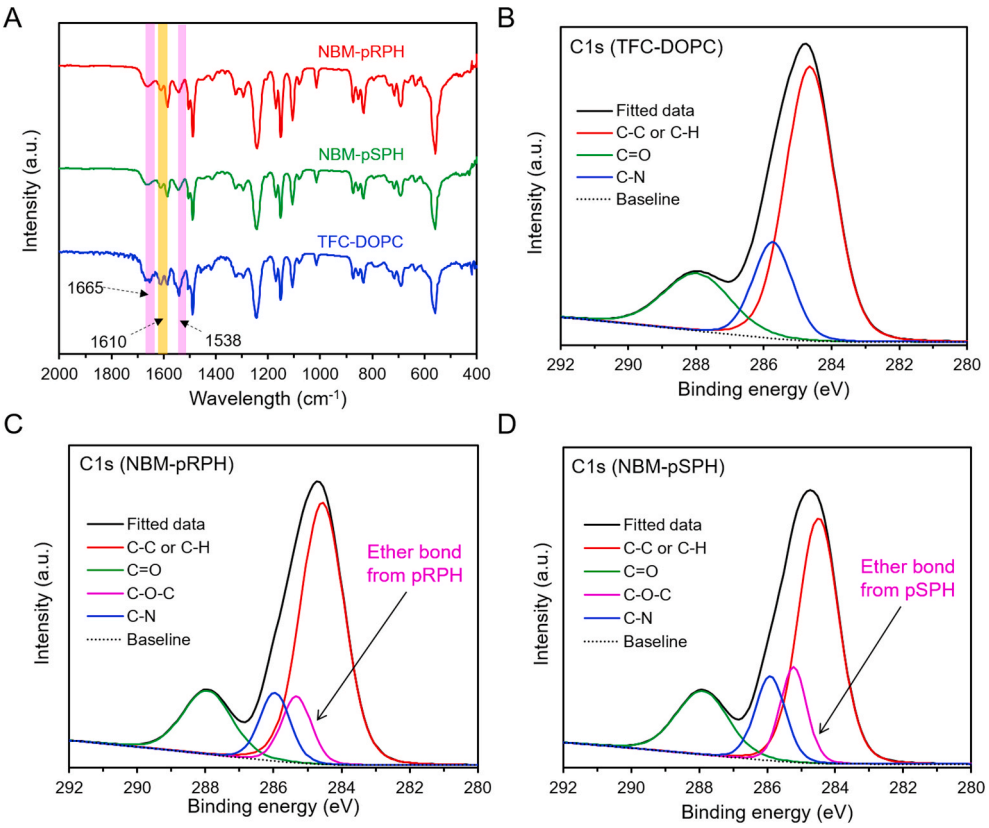

Fig. 6. (A) ATR-FTIR spectra from 2000-400 cm^{-1} for the TFC-DOPC, NBM-pRPH and NBM-pSPH membranes. High resolution C1s deconvoluted peaks in XPS for TFC-DOPC **(B)**, NBM-pRPH **(C)** and NBM-pSPH **(D)**. The liposome concentrations were fixed at 0.5 mg/mL in MPD solution for all three membranes. For NBM-pRPH and NBM-pSPH, the LCR is 200.

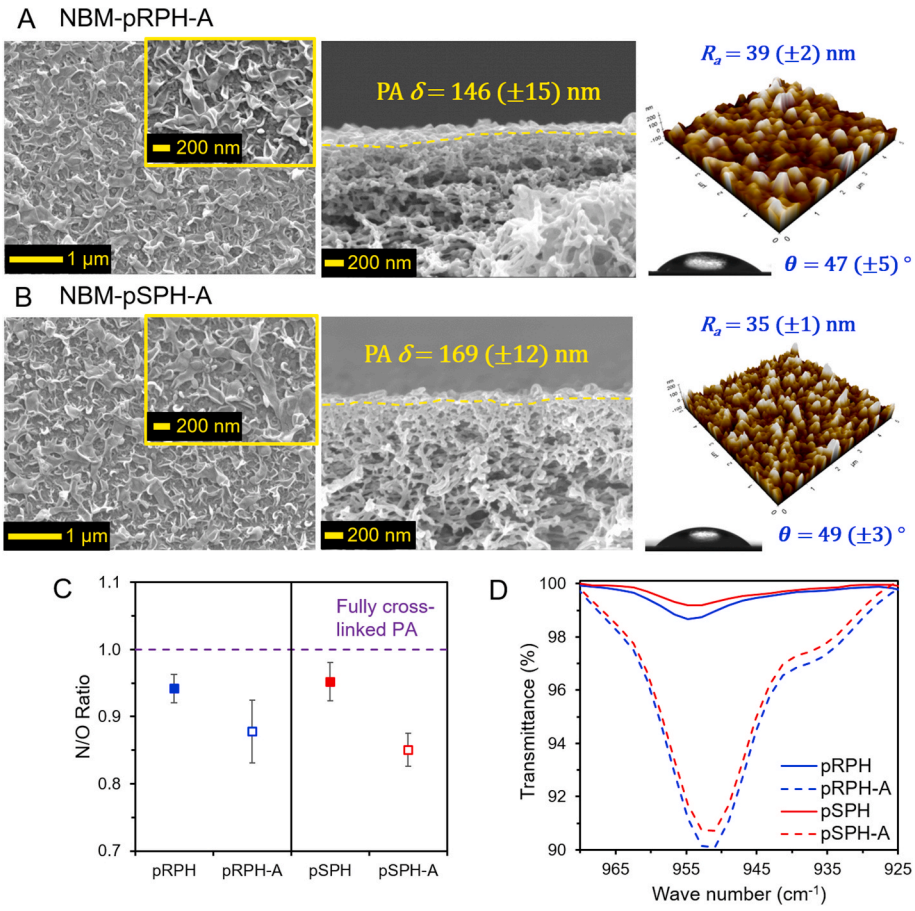

Fig. 7. The polyamide layer properties of the **(A)** NBM-pRPH-A and **(B)** NBM-pSPH-A membranes. The pRPH-/pSPH-liposome (LCR 200) concentration in MPD phase is 0.5 mg/mL. **Left images:** surface morphologies in SEM. **Middle images:** SEM cross-sectional images with the active layer height (δ). **Right images:** 3D AFM images with roughness average (R_a) and contact angle (θ) analysis. The cross-linking degrees of the four NBMs are presented in terms of: **(C)** N/O ratio obtained in XPS and **(D)** FTIR spectra at 950 cm^{-1}. Error bars: 3 or more independent samples.

and TMC can result in a lower extent of reaction between MPD and TMC monomers [23], and thus a lower polyamide cross-linking degree (*i.e.,* more free volumes in the polyamide network) [24]. This is further supported by the empirical evidence in Fig. 7D (intensity of the FTIR peak at 950 cm^{-1}) which shows a higher amount of unreacted acyl chloride groups for the NBMs made with additive, thereby reaffirming the reduction in cross-linking degree when DMSO additive was incorporated into the MPD aqueous phase [21,23,25]. In summary, it is concluded that the inclusion of the aqueous phase additives gave a thinner, smoother, looser and more hydrophilic active layer of the NBMs.

3.3. Desalination performances of the biomimetic membranes

3.3.1. Membranes without additives (TFC-DOPC, NBM-pRPH and NBM-pSPH)

Fig. 8A presents the desalination performance of the NBM-pRPH made with varying liposome concentrations. Overall, the biomimetic membranes were able to maintain a decent NaCl rejection of ~97.6–98.3% in all experimental runs (Fig. 8A and B), suggesting that minimal defects were introduced to the liposome-loaded polyamide layers. This is indeed plausible given that the vesicle size of ~120 nm is lower than that of the polyamide layer height (200–300 nm). Hence, the vesicles were fully embedded within the polyamide layer such that there

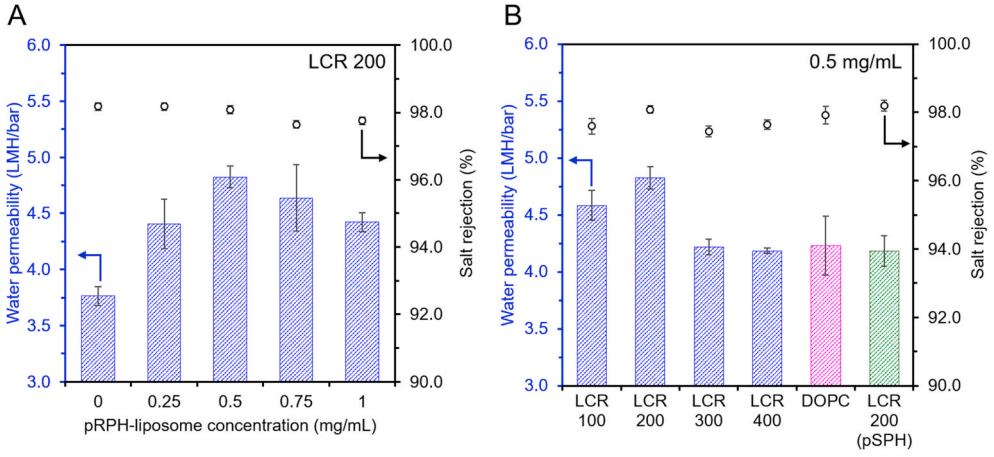

Fig. 8. (A) Water permeability and salt rejection of NBM-pRPH membranes prepared from different pRPH-liposome concentrations in MPD phase. The LCR of the pRPH-liposome was fixed at 200. **(B)** Water permeability and salt rejection of RO membranes prepared from different LCRs (pRPH-liposomes) (blue). The control membranes are the RO membranes made from DOPC liposomes (pink) and pSPH-liposomes (LCR 200) (green). The liposome concentration was fixed at 0.5 mg/mL in MPD aqueous phase. Error bars: 3 or more independent samples. The performances were obtained at 15.5 bar with 2000 ppm NaCl as feed. (For interpretation of the references to colour in this figure legend, the reader is referred to the Web version of this article.)

were no protruding vesicles on the polyamide surface as demonstrated by the TEM and STEM-EDX characterization results. As compared to the control membrane (liposome concentration is 0 mg/mL), the NBM-pRPH (pRPH-liposome concentration of 0.5 mg/mL) showed the highest permeability with a 28% increment (Fig. 8A). It is hypothesized that the lipid vesicles created more free volume in the active layer which explains the increase in water permeability as the liposome concentration was increased from 0 to 0.5 mg/mL. However, the water permeability did not increase proportionally with the liposome concentrations as evidenced by the drop in permeability for the NBM-pRPH loaded with a pRPH-liposome concentration of 1.0 mg/mL (Fig. 8A). This can be explained by the fact that the vesicles could have aggregated to form bigger globules, resulting in the formation of a thicker active layer (see Section 3.2.1). Consequently, this increased the hydraulic resistance for water permeation and thus the water permeability of NBM-pRPH decreased at high pRPH-liposome concentrations.

Based on the optimal pRPH-liposome concentration of 0.5 mg/mL (Fig. 8A), we further studied the effect of varying LCRs on the desalination performance of NBM-pRPH. Fig. 8B shows that the NBM-pRPH (LCR 200) showed 14% higher permeability as compared to the TFC membrane loaded with DOPC vesicles. It is also noticed that the NBM-pRPH membranes loaded with liposomes of LCRs 300/400 showed a similar water permeability to TFC-DOPC (~4.2 LMH/bar), which is plausible because of the low nanochannel loading in the vesicles.

To directly compare the flux improvement effect contributed by the water permeation property of the pRPH nanochannels, the performance of the NBM-pRPH and NBM-pSPH were compared at a fixed LCR 200 and liposome concentration of 0.5 mg/mL (Fig. 8B). The membrane loaded with the mutant pSPH (NBM-pSPH) had comparable water permeability (4.23 LMH/bar) to TFC-DOPC. On the other hand, the NBM-pRPH showed higher water permeability (4.82 LMH/bar) than the NBM-pSPH. Given that the polyamide matrices are fairly identical for NBM-pRPH and NBM-pSPH in terms of physical and chemical characteristics (see Section 3.2.1), the enhanced permeability of NBM-pRPH was attributed to the preferential passage through the synthetic nanochannels of pRPH-liposomes (Fig. 9), giving the water molecules accessibility to the hollow cores of the vesicles of lower hydrodynamic resistance. The impermeable nature of the DOPC liposomes and pSPH-liposomes means that water can only flow around the vesicles (*i.e.,* through the polyamide layer). On the other hand, the highly permeable nature of the pRPH-liposomes presents a possible supplementary transport pathway whereby water can flow through the liposomes (Fig. 9B) [37]. It is postulated that the supplementary water transport pathway enhances the water flux of the NBM-pRPH membrane when compared against TFC-DOPC and NBM-pSPH membranes.

3.3.2. Membranes with additives (NBM-pRPH-A and NBM-pSPH-A)

Table 1 outlines the desalination performances of our biomimetic membranes incorporated with aqueous phase additives (NBM-pRPH-A and NBM-pSPH-A). It is observed that both NBM-pRPH-A and NBM-pSPH-A showed much higher permeability (~26%) as compared to their counterparts made without additive (NBM-pRPH and NBM-pSPH). It is postulated that the higher permeability was achieved by a thinner, less cross-linked and more hydrophilic active layer (see Section 3.2.2), whereby the resistance for water transport across the active layer was significantly reduced for the NBMs incorporated with the additives [38]. More importantly, the NBM-pRPH-A showed ~10% higher permeability enhancement as compared to NBM-pSPH-A. Again, given that the polyamide matrices are rather identical for both membranes (see section 3.2.2), this is an unequivocal evidence that the higher permeability of NBM-pRPH-A with respect to NBM-pSPH-A stems from the preferential passage of water molecules through the pRPH synthetic nanochannels. It is also noticed from Table 1 that fairly similar permeability enhancements of ~12% were obtained by NBM-pRPH-A and NBM-pRPH against their mutant versions (NBM-pSPH-A and NBM-pSPH, respectively). In other words, with or without DMSO and TEACSA as additives, the increase in water permeability is believed to be attributed to the preferential transport of water molecules across the pRPH nanochannels. This suggests that both DMSO and TEACSA function primarily as additives in the IP process and do not have any effects (in terms of reaction or deformation) on the nanochannel-containing liposomes.

Table 1
Separation properties of the control (pristine TFC) membrane, TFC-DOPC and NBMs in this work. All performances were obtained under 15.5 bar of applied pressure and the feed solution was 2000 mg L^{-1} NaCl at 25 °C.

Membrane	*A* (LMH/bar)	R (%)	*B* (LMH)
Pristine TFC	3.76 ± 0.09	98.2 ± 0.5	0.97 ± 0.24
TFC-DOPC	4.23 ± 0.26	97.9 ± 0.3	1.25 ± 0.15
NBM-pRPH	4.82 ± 0.10	98.1 ± 0.1	1.32 ± 0.10
NBM-pSPH	4.18 ± 0.13	98.2 ± 0.2	1.07 ± 0.12
NBM-pRPH-A	6.09 ± 0.18	98.2 ± 0.3	1.54 ± 0.28
NBM-pSPH-A	5.57 ± 0.32	98.3 ± 0.2	1.32 ± 0.07

3.4. Empirical evidence of water transport through pRPH nanochannels

In this section, we attempt to provide more empirical evidence of the preferential water transport across the pRPH nanochannels during the brackish RO operation. The water flux of dense RO membranes exhibited a linear relationship with the applied feed pressure and temperature [39]. The water flux and salt rejection of the NBMs were measured at 15.5, 20, 25 and 30 bar (Fig. 10A and B, respectively). The water flux linearly increased with applied pressure in all cases (Fig. 10A). It is noticed that the membranes loaded with pRPH nanochannels showed a much higher rate of flux increase with feed pressure as compared to the membranes embedded with pSPH nanochannels. For example, the gradient (*m*) of the fitted lines for NBM-pRPH and NBM-pRPH-A were higher than NBM-pSPH and NBM-pSPH-A, respectively. A higher rate of

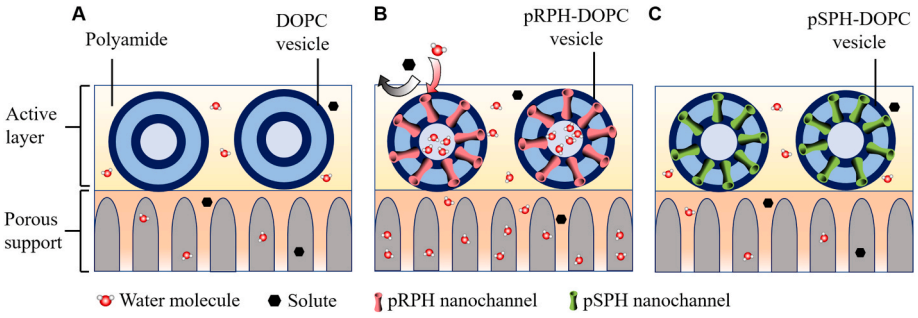

Fig. 9. The schematic illustration of the water transport across the RO membranes embedded with **(A)** DOPC liposomes, **(B)** pRPH-liposomes and **(C)** pSPH-liposomes. To ensure a fair comparison between these three membranes, the liposome concentration is fixed (*i.e.,* amount of vesicles added). The LCR (nanochannel load in the vesicles) were fixed for NBM-pRPH and NBM-pSPH to ensure a fair comparison between these two membranes.

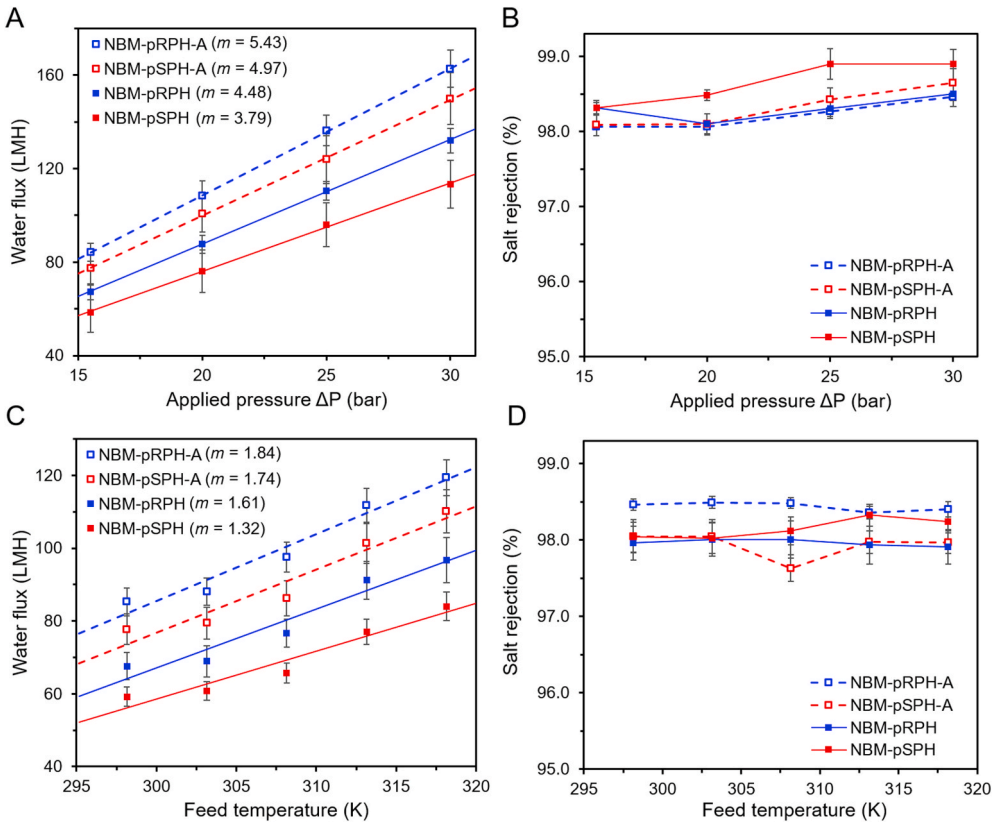

Fig. 10. Effect of pressure on the water flux **(A)** and salt rejection **(B)** of the tested RO membranes at constant feed temperature (25 °C). Effect of temperature on the water flux **(C)** and salt rejection **(D)** of the tested RO membranes at constant applied pressure (15.5 bar). The gradient (*m*) of the best-fit lines are presented for (A) and (C). The feed solution is 2000 ppm NaCl feed for all runs. Error bars: 3 independent samples.

flux increase with feed pressure implies that water transport through the nanochannels is accelerated by overcoming the entry resistance of pRPH nanochannels due to the increased pressure difference. This means that a larger amount of water molecules permeated through the pRPH nanochannels by overcoming the entry resistance due to the additional kinetic energy from the applied pressure, which is good evidence that water molecules diffused through the pRPH nanochannels embedded in the polyamide matrix [40,41]. On the other hand, the salt rejection increased slightly with the feed pressure (Fig. 10B), presumably because of the dilution effect whereby the water flux increase linearly at a constant salt flux. Also, the enhanced concentration polarization at higher flux can lead to a stronger electric bilayer that enabled the polyamide layer to reject salt more readily [8], which explains for the higher salt rejection at elevated pressures.

Secondly, the water flux of the NBMs in this study were measured as a function of feed temperature (Fig. 10C). It was observed that the NBM-pRPH and NBM-pRPH-A showed a higher rate of flux increase with feed temperature (*i.e.* higher gradient (*m*) of the fitted lines), as compared to NBM-pSPH and NBM-pSPH-A, respectively. It is postulated that water diffusion through the pRPH nanochannels is accelerated within its relatively smooth interior walls [6], and consequently the collision frequency between the diffusing water molecules and interior walls of the channel decreased at elevated temperature [40]. In addition, the drop in viscosity of water at a higher temperature is known to result in higher flux [42], and thus the higher rate of flux increase for NBM-pRPH and NBM-pRPH-A (compared to NBM-pSPH and NBM-pSPH-A, respectively) illuminates the possible water transport through the pRPH channels. On the other hand, the salt rejection remained fairly constant with increasing temperature (Fig. 10D) because the increase in water flux was offset by the increase in salt flux at higher feed temperatures. It is also noticed from Fig. 10A and C that flux enhancements of ~8–17% were obtained by NBM-pRPH-A and NBM-pRPH against their mutant versions (NBM-pSPH-A and NBM-pSPH, respectively) at elevated pressures (20–30 bar) and temperatures (30–45 °C), which is fairly similar to the ~9–15% flux enhancements obtained under initial testing conditions (15.5 bar and 25 °C). This is an indirect evidence that the nanochannel-containing liposomes are still intact (*i.e.,* do not deform) at elevated pressure and temperature (up to 30 bar and 45 °C, respectively).

3.5. Performance comparison of NBM-pRPH-A membrane with commercial membranes and RO membranes reported in literature

For comparison purposes, two commercial RO membranes (BW30 and ESPA2) were tested in parallel with our in-house made biomimetic membrane NBM-pRPH-A. Their performances are summarized in Table 2, alongside a list of RO membrane performances reported in the literature. Although it was not the purpose of this work to outperform commercial RO membranes in terms of water permeability, it is worth noting that the NBM-pRPH-A showed a relatively high water permeability while exhibiting a reasonable salt rejection as compared to the commercial RO membranes.

It is also noticed that a handful of TFC and thin-film nanocomposite (TFN) membranes showed even higher permeability than the NBM-pRPH-A, which means that there is still room for improvement for the NBM-pRPH-A membrane in terms of the permeability and/or selectivity. Notably, it is imperative to further improve the salt rejection capability of the NBM given that the membrane selectivity plays a crucial role in the removal of neutral solutes [43]. Nevertheless, this work potentially opens up another alternative pathway in the fabrication of nanochannel-based biomimetic membranes beyond AQPs with enhanced performance without significant compromise in selectivity.

Table 2
Desalination performances of membranes tested in this study, and flat-sheet RO membranes reported in the literature.

Membrane type	Testing coupon size (cm^2)	ΔP (bar)	Feed concentration (NaCl, ppm)	*A* (LMH/bar)	R (%)	Output	Ref., year
NBM-pRPH-A	42	15.5	2000	6.09 (±0.18)	98.2 (±0.3)	–	Current study
DuPont Filmtec BW30	42	15.5	2000	4.09 (±0.21)	97.5 (±0.4)	–	Tested in this study
Hydranautics ESPA2	42	15.5	2000	4.80 (±0.07)	98.7 (±0.1)	–	Tested in this study
AQP-based biomimetic	42	10	584	4.13 (±0.40)	97.2 (±0.6)	*J. Membr. Sci.*	[42], 2016
Polymersomes-based biomimetic	42	35	2000	2.40 (±0.20)	99.6 (±0.1)	*J. Membr. Sci.*	[20], 2018
Nanochannel-based biomimetic	22	18	5800	3.87 (±1.19)	99.7 (±0.1)	*Nature Nanotechnology*	[44], 2020
TFN with carbon nanotubes (CNTs)	42	15.5	2000	3.31 (±0.23)	98.5 (±0.1)	*Small*	[40], 2014
TFN with CNTs and graphene oxide	22.4	15.5	2000	4.23 (±0.14)	96.2	*J. Mat. Chem. A.*	[41], 2015
TFN with zeolite nanoparticles	28.6	15.5	2000	6.16 (±0.30)	98.4 (±0.2)	*J. Membr. Sci.*	[45], 2015
TFN with polymeric nanospheres	24	16	2000	4.94 (±0.21)	96.2 (±0.1)	*J. Membr. Sci.*	[46], 2020
TFN with zeolite imidazolate	18.5	15.5	2000	3.59 (±0.36)	99.0 (±0.1)	*J. Membr. Sci.*	[47], 2020
TFC with hydrophilic additives	28.6	15.5	2000	6.41	98.8	*Desalination*	[48], 2013
TFC with o-ABA-TEA salt	28.6	15.5	2000	7.36	98.4	*J. Membr. Sci.*	[49], 2013
TFC polyamide	34	15	2000	4.47 (±0.15)	98.8 (±0.2)	*J. Membr. Sci.*	[50], 2017
TFC polyamide	19.3	15.5	2000	4.75 (±0.13)	99.4 (±0.1)	*J. Membr. Sci.*	[51], 2017
TFC with polyisobutylene	19.6	15.5	2000	4.88 (±0.14)	98.4 (±0.2)	*J. Membr. Sci.*	[52], 2018
TFC with tannic acid	19.3	15.5	2000	3.59 (±0.14)	99.2 (±0.3)	*J. Membr. Sci.*	[53], 2018
TFC polyamide	28.3	15.5	2000	6.50 (±0.45)	99.3 (±0.1)	*J. Membr. Sci.*	[54], 2020
TFC polyamide	15.9	15	2000	3.74 (±0.10)	97.0 (±0.1)	*J. Membr. Sci.*	[55], 2020
TFC with cucurbit[6]uril	42	15.5	2000	4.01 (±0.11)	98.8 (±0.3)	*J. Membr. Sci.*	[25], 2020
TFC with zwitterionic molecules	28.3	15	2000	3.85 (±0.05)	98.5 (±0.1)	*J. Membr. Sci.*	[56], 2020
TFC with 1D nanochannels	22.5	16	2000	2.41 (±0.11)	97.3 (±0.6)	*J. Membr. Sci.*	[57], 2021
TFC with block copolymer surfactant	25	15.5	2000	1.69 (±0.05)	98.7 (±0.1)	*J. Membr. Sci.*	[58], 2021

4. Conclusions

This work demonstrates the feasibility of incorporating pRPH-liposomes into the active layer in the fabrication of NBMs. The optimized membrane, NBM-pRPH-A showed a 62% flux enhancement with respect to the basic control at similar salt rejection of 98.2%, thereby demonstrating the success in overcoming the trade-off between permeability and selectivity of RO membranes. More importantly, this work provides the basis for a comprehensive understanding of the liposome concentration, LCR and the aqueous phase additives in the fabrication of biomimetic RO membranes with enhanced permselectivity. Several conclusions can be derived from this study:

(1) The NBM-pRPH membrane prepared with a liposome concentration of 0.5 mg/mL (LCR 200) showed enhanced permeability (28%) with respect to the TFC control membrane.
(2) The NBMs incorporated with the additives (*e.g.* NBM-pRPH-A) showed further permeability enhancement (26%) from the NBM-pRPH membranes. This is postulated to be achieved by a thinner, less cross-linked and more hydrophilic active layer.
(3) In all optimizations, the salt rejection of the biomimetic membranes were maintained at ~97.6–98.5%, thereby reaffirming that the incorporation of liposomes did not induce defects onto the polyamide layer.
(4) The STEM-EDX characterization revealed that the liposomes were successfully incorporated into the polyamide layer of the biomimetic membranes.
(5) The RO tests of the biomimetic membranes under differential pressures and temperatures provide empirical evidence of the preferential water transport across the pRPH nanochannels embedded within lipid bilayers.

Authors statement

Yu Jie Lim: Conceptualization, Investigation, Data curation, Writing - Original Draft.
Kunli Goh: Investigation, Conceive Data, Writing - review & editing.
Gwo Sung Lai: Conceptualization, Methodology, Resources.
Chiann Yi Ng: Visualization, Investigation.
Jaume Torres: Supervision.
Rong Wang: Supervision, Writing - review & editing, Project administration, Funding acquisition.

CRediT authorship contribution statement

Yu Jie Lim: Conceptualization, Investigation, Data curation, Writing – original draft. **Kunli Goh:** Investigation, Conceive Data, Writing – review & editing. **Gwo Sung Lai:** Conceptualization, Methodology, Resources. **Chiann Yi Ng:** Visualization, Investigation. **Jaume Torres:** Supervision. **Rong Wang:** Supervision, Writing – review & editing, Project administration, Funding acquisition.

Declaration of competing interest

The authors declare that they have no known competing financial interests or personal relationships that could have appeared to influence the work reported in this paper.

Acknowledgements

This research grant was supported by the Singapore National Research Foundation under its Environment and Water Research Program and administered by PUB, Singapore's National Water Agency (grant number: 1501-IRIS-04). We would like to acknowledge Ms. Janelle Ng from NEWRI Analytics Cluster, Nanyang Technological University, Singapore, for the guidance in operating XPS and TEM in membrane characterization. We would also like to acknowledge Mr. Song Zhijian from the Singapore Membrane Technology Centre, Nanyang Technological University, Singapore, for the assistance in the synthesis of nanochannels in this work. The funding support from the Economic Development Board of Singapore to the Singapore Membrane Technology Center, Nanyang Environment and Water Research Institute, Nanyang Technological University is gratefully acknowledged.

References

[1] P. Greve, T. Kahil, J. Mochizuki, T. Schinko, Y. Satoh, P. Burek, G. Fischer, S. Tramberend, R. Burtscher, S. Langan, Global assessment of water challenges under uncertainty in water scarcity projections, Nat. Sustain. 1 (2018) 486–494.
[2] K.P. Lee, T.C. Arnot, D. Mattia, A review of reverse osmosis membrane materials for desalination—development to date and future potential, J. Membr. Sci. 370 (2011) 1–22.
[3] G.M. Geise, H.B. Park, A.C. Sagle, B.D. Freeman, J.E. McGrath, Water permeability and water/salt selectivity tradeoff in polymers for desalination, J. Membr. Sci. 369 (2011) 130–138.
[4] Z. Yang, H. Guo, C.Y. Tang, The upper bound of thin-film composite (TFC) polyamide membranes for desalination, J. Membr. Sci. 590 (2019) 117297.
[5] D. Cohen-Tanugi, R.K. McGovern, S.H. Dave, J.H. Lienhard, J.C. Grossman, Quantifying the potential of ultra-permeable membranes for water desalination, Energy Environ. Sci. 7 (2014) 1134–1141.
[6] J.R. Werber, C.O. Osuji, M. Elimelech, Materials for next-generation desalination and water purification membranes, Nat. Rev. Mater. 1 (2016) 16018.
[7] Z. Yang, X.-H. Ma, C.Y. Tang, Recent development of novel membranes for desalination, Desalination 434 (2018) 37–59.
[8] K. Goh, H.E. Karahan, L. Wei, T.-H. Bae, A.G. Fane, R. Wang, Y. Chen, Carbon nanomaterials for advancing separation membranes: a strategic perspective, Carbon 109 (2016) 694–710.
[9] J.R. Werber, C.J. Porter, M. Elimelech, A path to ultraselectivity: support layer properties to maximize performance of biomimetic desalination membranes, Environ. Sci. Technol. 52 (2018) 10737–10747.
[10] A.G. Fane, R. Wang, M.X. Hu, Synthetic membranes for water purification: status and future, Angew. Chem. Int. Ed. 54 (2015) 3368–3386.
[11] Y.-x. Shen, P.O. Saboe, I.T. Sines, M. Erbakan, M. Kumar, Biomimetic membranes: a review, J. Membr. Sci. 454 (2014) 359–381.
[12] C.J. Porter, J.R. Werber, M. Zhong, C.J. Wilson, M. Elimelech, Pathways and challenges for biomimetic desalination membranes with sub-nanometer channels, ACS Nano 14 (2020) 10894–10916.
[13] Y.-M. Tu, L. Samineni, T. Ren, A.B. Schantz, W. Song, S. Sharma, M. Kumar, Prospective applications of nanometer-scale pore size biomimetic and bioinspired membranes, J. Membr. Sci. (2020) 118968.
[14] X.-B. Hu, Z. Chen, G. Tang, J.-L. Hou, Z.-T. Li, Single-molecular artificial transmembrane water channels, J. Am. Chem. Soc. 134 (2012) 8384–8387.
[15] Y.-x. Shen, W. Si, M. Erbakan, K. Decker, R. De Zorzi, P.O. Saboe, Y.J. Kang, S. Majd, P.J. Butler, T. Walz, Highly permeable artificial water channels that can self-assemble into two-dimensional arrays, Proc. Natl. Acad. Sci. Unit. States Am. 112 (2015) 9810–9815.
[16] Q. Li, X. Li, L. Ning, C.H. Tan, Y. Mu, R. Wang, Hyperfast water transport through biomimetic nanochannels from peptide-attached (pR)-pillar[5]arene, Small 15 (2019) 1804678.
[17] L. Chen, W. Si, L. Zhang, G. Tang, Z.-T. Li, J.-L. Hou, Chiral selective transmembrane transport of amino acids through artificial channels, J. Am. Chem. Soc. 135 (2013) 2152–2155.
[18] Y.-x. Shen, W. Song, D.R. Barden, T. Ren, C. Lang, H. Feroz, C.B. Henderson, P. O. Saboe, D. Tsai, H. Yan, Achieving high permeability and enhanced selectivity for Angstrom-scale separations using artificial water channel membranes, Nat. Commun. 9 (2018) 1–11.
[19] Y. Li, S. Qi, M. Tian, W. Widjajanti, R. Wang, Fabrication of aquaporin-based biomimetic membrane for seawater desalination, Desalination 467 (2019) 103–112.
[20] S. Qi, W. Fang, W. Siti, W. Widjajanti, X. Hu, R. Wang, Polymersomes-based high-performance reverse osmosis membrane for desalination, J. Membr. Sci. 555 (2018) 177–184.
[21] Y.J. Lim, J. Lee, T.-H. Bae, J. Torres, R. Wang, Feasibility and performance of a thin-film composite seawater reverse osmosis membrane fabricated on a highly porous microstructured support, J. Membr. Sci. (2020) 118407.
[22] J. Lee, R. Wang, T.-H. Bae, High-performance reverse osmosis membranes fabricated on highly porous microstructured supports, Desalination 436 (2018) 48–55.
[23] J. Lee, R. Wang, T.-H. Bae, A comprehensive understanding of co-solvent effects on interfacial polymerization: interaction with trimesoyl chloride, J. Membr. Sci. 583 (2019) 70–80.
[24] B. Khorshidi, T. Thundat, D. Pernitsky, M. Sadrzadeh, A parametric study on the synergistic impacts of chemical additives on permeation properties of thin film composite polyamide membrane, J. Membr. Sci. 535 (2017) 248–257.
[25] J. Lee, F. Zhou, K. Baek, W. Kim, H. Su, K. Kim, R. Wang, T.-H. Bae, Use of rigid cucurbit[6]uril mediating selective water transport as a potential remedy to improve the permselectivity and durability of reverse osmosis membranes, J. Membr. Sci. (2020) 119017.
[26] C. Van Goethem, R. Verbeke, M. Pfanmöller, T. Koschine, M. Dickmann, T. Timpel-Lindner, W. Egger, S. Bals, I.F. Vankelecom, The role of MOFs in thin-film nanocomposite (TFN) membranes, J. Membr. Sci. 563 (2018) 938–948.
[27] H. Zheng, Z. Mou, K. Zhou, Incorporation of core–shell-structured zwitterionic carbon dots in thin-film nanocomposite membranes for simultaneously improved perm-selectivity and antifouling properties, ACS Appl. Mater. Interfaces 12 (2020) 53215–53229.
[28] Y. Kaufman, A. Berman, V. Freger, Supported lipid bilayer membranes for water purification by reverse osmosis, Langmuir 26 (2010) 7388–7395.
[29] J. Duan, E. Litwiller, I. Pinnau, Preparation and water desalination properties of POSS-polyamide nanocomposite reverse osmosis membranes, J. Membr. Sci. 473 (2015) 157–164.
[30] B. Khorshidi, T. Thundat, B.A. Fleck, M. Sadrzadeh, A novel approach toward fabrication of high performance thin film composite polyamide membranes, Sci. Rep. 6 (2016) 22069.
[31] Q. Zhang, Z. Zhang, L. Dai, H. Wang, S. Li, S. Zhang, Novel insights into the interplay between support and active layer in the thin film composite polyamide membranes, J. Membr. Sci. 537 (2017) 372–383.
[32] W. Yan, Z. Wang, J. Wu, S. Zhao, J. Wang, S. Wang, Enhancing the flux of brackish water TFC RO membrane by improving support surface porosity via a secondary pore-forming method, J. Membr. Sci. 498 (2016) 227–241.
[33] X. Li, Q. Li, W. Fang, R. Wang, W.B. Krantz, Effects of the support on the characteristics and permselectivity of thin film composite membranes, J. Membr. Sci. 580 (2019) 12–23.
[34] X. Kong, Z.-L. Qiu, C.-E. Lin, Y.-Z. Song, B.-K. Zhu, L.-P. Zhu, X.-Z. Wei, High permselectivity hyperbranched polyester/polyamide ultrathin films with nanoscale heterogeneity, J. Mater. Chem. 5 (2017) 7876–7884.
[35] J. Xiang, Z. Xie, M. Hoang, K. Zhang, Effect of amine salt surfactants on the performance of thin film composite poly (piperazine-amide) nanofiltration membranes, Desalination 315 (2013) 156–163.
[36] A. Rahimpour, M. Jahanshahi, M. Peyravi, S. Khalili, Interlaboratory studies of highly permeable thin-film composite polyamide nanofiltration membrane, Polym. Adv. Technol. 23 (2012) 884–893.
[37] K. Goh, L. Setiawan, L. Wei, W. Jiang, R. Wang, Y. Chen, Fabrication of novel functionalized multi-walled carbon nanotube immobilized hollow fiber membranes for enhanced performance in forward osmosis process, J. Membr. Sci. 446 (2013) 244–254.
[38] M.R. Chowdhury, J. Steffes, B.D. Huey, J.R. McCutcheon, 3D printed polyamide membranes for desalination, Science 361 (2018) 682–686.
[39] J.G. Wijmans, R.W. Baker, The solution-diffusion model: a review, J. Membr. Sci. 107 (1995) 1–21.
[40] H.D. Lee, H.W. Kim, Y.H. Cho, H.B. Park, Experimental evidence of rapid water transport through carbon nanotubes embedded in polymeric desalination membranes, Small 10 (2014) 2653–2660.
[41] H.J. Kim, M.-Y. Lim, K.H. Jung, D.-G. Kim, J.-C. Lee, High-performance reverse osmosis nanocomposite membranes containing the mixture of carbon nanotubes and graphene oxides, J. Mater. Chem. 3 (2015) 6798–6809.
[42] S. Qi, R. Wang, G.K.M. Chaitra, J. Torres, X. Hu, A.G. Fane, Aquaporin-based biomimetic reverse osmosis membranes: stability and long term performance, J. Membr. Sci. 508 (2016) 94–103.
[43] J.R. Werber, A. Deshmukh, M. Elimelech, The critical need for increased selectivity, not increased water permeability, for desalination membranes, Environ. Sci. Technol. Lett. 3 (2016) 112–120.
[44] M. Di Vincenzo, A. Tiraferri, V.-E. Musteata, S. Chisca, R. Sougrat, L.-B. Huang, S. P. Nunes, M. Barboiu, Biomimetic artificial water channel membranes for enhanced desalination, Nat. Nanotechnol. (2020) 1–7.

[45] H. Dong, L. Zhao, L. Zhang, H. Chen, C. Gao, W.W. Ho, High-flux reverse osmosis membranes incorporated with NaY zeolite nanoparticles for brackish water desalination, J. Membr. Sci. 476 (2015) 373–383.
[46] Y. Wang, H. Zhang, C. Song, C. Gao, G. Zhu, Effect of aminophend/formaldehyde resin polymeric nanospheres as nanofiller on polyamide thin film nanocomposite membranes for reverse osmosis application, J. Membr. Sci. 614 (2020) 118496.
[47] P. Li, M. Zhang, Z. Zhai, M. Wang, P. Li, Y. Hou, Q.J. Niu, Precise assembly of a zeolite imidazolate framework on polypropylene support for the fabrication of thin film nanocomposite reverse osmosis membrane, J. Membr. Sci. 612 (2020) 118412.
[48] L. Zhao, P.C.-Y. Chang, W.W. Ho, High-flux reverse osmosis membranes incorporated with hydrophilic additives for brackish water desalination, Desalination 308 (2013) 225–232.
[49] L. Zhao, P.C.-Y. Chang, C. Yen, W.W. Ho, High-flux and fouling-resistant membranes for brackish water desalination, J. Membr. Sci. 425 (2013) 1–10.
[50] J. Xu, H. Yan, Y. Zhang, G. Pan, Y. Liu, The morphology of fully-aromatic polyamide separation layer and its relationship with separation performance of TFC membranes, J. Membr. Sci. 541 (2017) 174–188.
[51] M. Shi, Z. Wang, S. Zhao, J. Wang, S. Wang, A support surface pore structure reconstruction method to enhance the flux of TFC RO membrane, J. Membr. Sci. 541 (2017) 39–52.
[52] S. Wang, Y. Zhou, C. Gao, Novel high boron removal polyamide reverse osmosis membranes, J. Membr. Sci. 554 (2018) 244–252.
[53] M. Shi, Z. Wang, S. Zhao, J. Wang, P. Zhang, X. Cao, A novel pathway for high performance RO membrane: preparing active layer with decreased thickness and enhanced compactness by incorporating tannic acid into the support, J. Membr. Sci. 555 (2018) 157–168.
[54] M. Shi, W. Yan, Y. Zhou, Z. Wang, L. Liu, S. Zhao, Y. Ji, J. Wang, C. Gao, P. Zhang, Combining tannic acid-modified support and a green co-solvent for high performance reverse osmosis membranes, J. Membr. Sci. 595 (2020) 117474.
[55] Z. Zhang, Y. Qin, G. Kang, H. Yu, Y. Jin, Y. Cao, Tailoring the internal void structure of polyamide films to achieve highly permeable reverse osmosis membranes for water desalination, J. Membr. Sci. 595 (2020) 117518.
[56] X. Shan, S.-L. Li, W. Fu, Y. Hu, G. Gong, Y. Hu, Preparation of high performance TFC RO membranes by surface grafting of small-molecule zwitterions, J. Membr. Sci. (2020) 118209.
[57] W.-x. Li, Z. Yang, W.-l. Liu, Z.-h. Huang, H. Zhang, M.-p. Li, X.-h. Ma, C.Y. Tang, Z.-l. Xu, Polyamide reverse osmosis membranes containing 1D nanochannels for enhanced water purification, J. Membr. Sci. 618 (2021) 118681.
[58] K.H. Jung, H.J. Kim, M.H. Kim, H. Seo, J.-C. Lee, Superamphiphilic zwitterionic block copolymer surfactant-assisted fabrication of polyamide thin-film composite membrane with highly enhanced desalination performance, J. Membr. Sci. 618 (2021) 118677.